

Concept design of a high power superconducting generator for future hybrid-electric aircraft

Mykhaylo Filipenko¹ , Lars Kühn¹, Thomas Gleixner¹, Martin Thummet¹, Marc Lessmann¹, Dirk Möller¹, Matthias Böhm¹, Andreas Schröter¹, Kerstin Häse¹, Jörn Grundmann², Markus Wilke², Michael Frank², Peter van Hasselt², Johannes Richter², Mercedes Herranz-Garcia², Christian Weidemann², Arestid Spangolo² and Markus Klöpzig²

¹Rolls-Royce Deutschland Ltd. & Co. KG, Germany

²Siemens AG, Corporate Technology, Germany

E-mail: mykhaylo.filipenko@rolls-royce.com

Received 24 October 2019, revised 13 December 2019

Accepted for publication 8 January 2020

Published 16 March 2020



CrossMark

Abstract

The reduction of emission is a key goal for the aviation industry. One enabling technology to achieve this goal, could be the transition from conventional gas turbines to hybrid-electric drive trains. However, the requirements concerning weight and efficiency that come from applications like short range aircraft are significantly higher than what state-of-the-art technology can offer. A key technology that potentially allows to achieve the necessary power and volume densities for rotating electric machines is superconductivity. In this paper we present the concept of a high power density generator that matches the speed of typical airborne turbines in its power class. The design is based on studies that cover topology selection and further electromagnetic, HTS, thermal, structural and cryogenics aspects. All domains were analyzed by means of analytical sizing and 2D/3D FEA modeling. With the help of our digital twin that is a synthesis of these models, we can demonstrate for the first time that under realistic assumptions on material properties gravimetric power densities beyond 20 kW kg^{-1} can be achieved.

Keywords: hybrid-electric aircraft propulsion, application of superconductivity, electric machines, high power density, liquid hydrogen, high voltage

(Some figures may appear in colour only in the online journal)

1. Introduction

The contribution of the aviation industry to total global emissions is about 2% [1]. Although this number does not appear to be huge, the effects of this emissions on the climate cannot be underestimated as they are released in high altitude and therefore have a much stronger effect on the shielding top layers of the atmosphere compared to emissions released

close the surface. With an annual growth rate of 5% per year, the aviation industry will double its emissions until 2050 if no actions are taken. Thus, the commission of the European Union, together with the major players of the industry, formulated a roadmap titled Flightpath 2050 [2] according to which CO₂ emission have to be reduced by 75%, NO_x emissions by 90% and noise emissions by 80%.

As discussed previously by many authors [3, 4] these ambitious goals can only partially be achieved by gradually improving conventional turbine technology. Besides bio-fuels, electric propulsion systems for small aircraft and hybrid electric propulsion systems (HEPS) for regional and short range aircraft are regarded as major drivers for the



Original content from this work may be used under the terms of the [Creative Commons Attribution 4.0 licence](https://creativecommons.org/licenses/by/4.0/). Any further distribution of this work must maintain attribution to the author(s) and the title of the work, journal citation and DOI.

reduction of noise pollution and green-house gas emissions. Purely electric propulsion systems clearly suffers from energy density of available electric storage technologies wherefore in the near future only applications with limited flight range seem to be realistic. For short range aircraft (A320 class), which has a market share of roughly 70% in the commercial aviation market [5] and therefore the largest emission contribution, battery energy densities of over 1 kWh kg^{-1} are required for practical use [6, 7] which does not appear achievable according to current roadmaps on battery development [8].

A prerequisite for short range aircraft with HEPS, are electric components (electric machines, power electronics etc) than can meet the ambitious weight and efficiency requirements for this application. For instance, for the N3X concept aircraft power densities of at least 13.7 kW kg^{-1} are required [9]. Current state-of-the-art electric components in the multi-MW power class could potentially meet the efficiency requirements but are roughly a factor of 50–100 too heavy in order to be used for a HEPS in aircraft. As initial studies [10] show a weight reduction by a factor of about 10 could be achieved by means of enhanced cooling techniques and lightweight design that was not applied for industrial electrical machines so far. However, to bridge another gap of about 5–10, more radical approaches are necessary. A potential technology to make that leap for rotating electric machines is high temperature superconductivity (HTS). While the best permanent magnets can have a magnetization of up to 1.3 T, superconducting coils made from HTS-tapes or magnets made from bulk HTS material can produce magnetic field densities up to 14 T [11] at their surface. Further, current densities over 200 A mm^{-2} can easily be achieved in HTS tapes or MgB_2 wires [12]. As the gravimetric power density of electric machines scales linearly with the magnetic field density in the airgap and the stator current loading, a factor of 5–10 seems to be feasible looking at the numbers given before.

Following this promise, numerous machines have been built and tested to demonstrate the general feasibility of electric machines based on HTS [13, 14]. In particular, prototypes for marine and wind-generation application have been realized successfully [15–18]. A comprehensive overview can be found in [19, 20]. However, only few concepts have been realized or studied in detail to meet the weight and efficiency targets of passenger aircraft [21–23]. Thus, it is valuable to analyze what is achievable with HTS technology after a thorough machine design is done for requirements that are typical for short range aircraft. In this paper we present our results on performing this analysis.

The paper is structured as follows: first, we present the consideration behind the specifications for our generator design that could be used in a future HEPS (section 2). Based on these specification we performed a topology trade-off analysis (section 3) and detailed studies on electromagnetic behavior, structural integrity, thermal management (section 4) accompanied by dedicated experiments (section 5). Finally, we can conclude that the digital twin which we built up for our design indicates that the realization of a generator with

Table 1. Baseline specification for generator design study.

Mechanical power at shaft	$P = 10 \text{ MW}$
Rotation speed at shaft	$n_{rot} = 7\,000 \text{ rpm}$
Efficiency at nominal operation	$\eta > 98\%$
DC-link voltage	$U_{DC} = 3 \text{ kV}$
Stray field in 1 m distance	$B_{stray} < 0.5 \text{ mT}$

power densities over 20 kW kg^{-1} is doable but challenging in terms of materials and manufacturing.

2. Generator specifications

As outlined in the introduction, we take the short range aircraft class as a basis for the considerations in this paper. We derived meaningful specifications for our generator study according to following reasoning: the A320 has two engines that can provide a maximum total power of 40 MW during take-off and roughly 20 MW in cruise altitude. Typically in a HEPS architecture during take-off, half of the electric power to the propulsion units would be provided by the GenSets (generator plus turbine) and the other half by the batteries. Due to redundancy a split into at least two GenSet units of 10 MW is reasonable. Thus, we used 10 MW as a baseline for the power rating of the generator.

In order to determine a meaningful rotation speed at the shaft, we generated a survey of available airborne gas turbines with a power of roughly 10 MW and found that the rotation speed ranges roughly from 5 500 rpm to 11 000 rpm for gas turbines in that power class. As both for the generator and the gas turbine the power density in general increases with higher rotation speeds, it is reasonable to eliminate the gearbox and couple the generator directly to the turbine. We chose a speed of 7 000 rpm as baseline as it is harder to achieve high power densities with lower rotation speed and the majority of turbines had its coupling shaft rotation speed around this value.

Further, for the voltage level we took as an orientation what was proposed by other authors [24, 25] and decided to set the DC voltage to 3 kV. We would like to mention that this value is more an educated guess that serves as a starting point for further considerations rather than a quantitatively elaborated value due to profound system studies. Nevertheless, looking into cable weight models one can find out that the weight-per-meter of DC cable does not decrease much anymore by increasing the voltage over 3 kV. Hence, 3 kV could be a reasonable trade-off between weight and safety concerning the cable.

For the efficiency we decided to set a goal of $\eta > 98\%$ as proposed by NASA [9]. This goal marks an intermediate step towards going to higher efficiencies above 99%. As a last specification we took into account that the stray field in a distance larger than 1 m away from the machine should be smaller than 0.5 mT as required by [26]. All specifications are summarized in table 1.

3. Preconsideration on materials and topology studies

As a starting point for our pre-sizing and following detailed study, we fixed the following pre-requisites on technology, materials and state-of-the-art in manufacturing:

- (i) We consider liquid hydrogen as the cooling liquid at a temperature of about 20 K for the rotor. We do not restrict the amount of hydrogen that is required for cooling but design with the mindset of minimizing the losses in the cold. This consideration resides from a scenario where a cryo-cooler is used or the liquid hydrogen is stored only for the purpose of cooling, so that the losses will translate directly into additional system mass.
- (ii) As a practically usable high-temperature superconducting material we consider HTS-tapes that can be wound to coils. Such coils could be put in the rotor or stator in principle. For the rotor coils, we assume an operating current density of about 300 A mm^{-2} in the coils. This performance can be realized with currently available HTS-material [27, 28].
- (iii) In the stator the HTS-tapes are subject to high frequency AC-currents that lead to significant AC-losses. A rough estimation of these losses reveals that the efficiency target would not be met. MgB_2 wires could pose a possible option to this problem but as we there is no documented experience with high current, high voltage, high frequency MgB_2 based stator coils we did not look further into this option as a part of this study. Nevertheless, this could be an attractive option in a further development.
- (iv) As the stator is not cold but warm, assumptions on the current density in the copper conductor have to be made for pre-sizing. As we know from previous projects, liquid direct cooling is a realistic option that can provide high densities. According to literature [29], a current density up to 25 A mm^{-2} is realistic.
- (v) For liquid cooling we assume an inlet temperature of 90°C as a reasonable trade-off (based on engineering judgment) between generator cooling (which is easier with a cooler liquid) and the mass of the heat exchanger that is required for re-cooling of the liquid.
- (vi) Due to practical experience with HTS-bulks [30] we consider them as a potential alternative to HTS-tape coils in order to create a magnetic field in the rotor. As the highest trapped field 20 K with field cooling is reported to be around 15 T [11], we assumed that roughly 5 T trapped field could be achievable for practical applications. Further research to achieve such magnetic field densities is required as currently only up to 4.8 T could be achieved in experiments with single bulks [31].
- (vii) For the stator and rotor yoke we consider FeCo. Albeit its high price it offers the highest saturation magnetization at reasonable losses if used as laminated steel such as offered by Vakuumschmelze [32].

- (viii) We limit the electric frequency of the fundamental current waveform to roughly 1 kHz as already 100 Hz is a challenge for inverters in this power class and frequencies above 1 kHz appeared to be unrealistic in this power class according to our engineering judgment.

Before going into a quantitative pre-sizing, we excluded particular topologies from a further quantitative pre-sizing due to the following qualitative considerations:

- *DC machines:* Although DC-machines have some inherently attractive properties in particular in connection with superconductors, we excluded DC-machines from our considerations. According to our knowledge state-of-the-art DC-brushes for high currents are maintenance intensive, have a low-life time and have usually high contact losses leading to low efficiency. Thus, we expect this component solely to outweigh the rest of the machine and therefore to be a severe show-stopper for this concept.
- *Induction machines:* Induction machines are in general known to be heavier than synchronous machines as the magnetic field of the rotor of an induction machine is lower than of the field of a wound machine or a machine with permanent magnets. Nevertheless, one could think about an induction machine with HTS-tapes as due to the high current densities that are possible in HTS-tapes the copper weight would reduce drastically. Although some positive results have been achieved with low-power prototype based on MgB_2 , two problems arise: As the superconductor has no DC-losses, the asynchronous machine becomes a synchronous machine at some point. However, the excitation field from the stator is not strong enough to create such a strong excitation in the rotor that it can compete with an HTS-bulk or a wounded pole. The second problem is that induction machine usually require a very small magnetic airgap to maximize its performance. That does not go well with a superconducting rotor that requires extra space in the mechanical airgap for vacuum insulation.
- *Axial flux machines:* The torque of axial flux machines scales either with the diameter of the rotor discs or multiple rotor discs have to be stacked. Axial flux machines are well-known for applications in the 40–300 kW range [33, 34]. When scaling such machines to high speed and high power, the size of discs is inherently limited by centrifugal forces. Further, thin plates with large diameters have severe issues with rotordynamics. Providing sufficient stiffness results in high rotor masses. Thus, multiple stacked rotor discs have to be used which increase the machine's complexity and also results in larger masses. Therefore, we rejected this machine topology due to the high power requirement of 10 MW.
- *Transversal flux machines:* Although the transversal flux topology could be a good candidate to achieve high power densities, this topology has usually a sophisticated magnetic circuit with much non-saturated soft-magnetic material for flux guidance. This material is the major contributor its active parts mass. High magnetic field densities excited by HTS coils or bulks will either saturate the soft-magnetic material or require overproportionally

Table 2. An overview over the best machine designs concerning power density for the pre selected topologies.

Topology	IR-SPM	IR-SPM air-core	OR-SPM air-core	OR-SPM no-yoke	IR HTS-bulk	OR HTS-bulk	IR HTS-wound
Outer radius stator (mm)	286	292	262	263	252	195	290
Inner radius stator (mm)	269	259	229	231	204	169	253
Outer radius rotor (mm)	250	250	291	29772	195	228	183
Inner radius rotor (mm)	230	230	271	272	180	203	140
Axial length (mm)	680	700	620	600	250	266	157
Magnet height (mm)	10	10	20	25	15	25	42
Airgap (mm)	9	9	9	9	9	9	30
Torque (kNm)	14.0	14.0	14.0	14.0	13.9	13.8	14.1
Current (kA rms)	4.9	4.9	4.9	4.9	3.2	3.2	2.5
Voltage per phase (V rms)	1196	1360	840	856	1024	1066	1750
$\cos \phi$	0.57	0.46	0.46	0.46	0.95	0.99	0.72
Efficiency (%)	97.7	97.8	97.8	97.8	99.1	99.5	98.4
Active part mass (kg)	351	427	347	316	129	96	158
Active part power density (kW kg ⁻¹)	28.5	23.4	28.8	31.6	77.5	104.6	64.8

large soft-magnetic material parts making the magnetic circuit even heavier. Thus, the transversal flux topology does not appear to be the best fit for HTS.

- *Flux switching machines:* A similar argument applies to flux switching machines as to transversal flux machines: as the topology is dependent on the soft-magnetic material for flux guidance, HTS does not appear to be a proper match for this topology.
- *Reluctance machines:* We did not look further into reluctance machines as such machines do not have any excitation field in the rotor and we excluded cryo-stators from this study for the reasons explained above.

We used the analytic sizing tool SPEED 13.04.011 to compare quantitatively the remaining options, namely: synchronous permanent magnet (SPM) radial flux machine with inner and/or outer rotor, synchronous machine with wound field HTS-tape poles, SPM radial flux machine with inner and/or outer rotor with HTS-bulks as magnets. For the SPM machines (with HTS-bulks and NeFeB magnets) we used the PC-BDC module of SPEED and for the wound field variant we used PC-WFC.

HTS-bulks were modeled as permanent magnets with an extraordinary magnetization of 5 T. Although, this is obviously far from reality, it gives a good starting point for pre-sizing comparison. As shown in [35], the deviation of the resulting torque due to the different shape of the magnetic field of a HTS-bulk compared to a NeFeB permanent magnet is in the range of 10%. HTS-coils in the rotor were modeled as copper coils with a current density of roughly 300 A mm⁻² and the thermal losses were neglected. The permanent magnets for SPM were NeFeB magnets with material parameters according to [36] (i.e. 1.3 T magnetization).

For all designs including HTS-material we choose an air-gap of 30 mm as this is a good estimate to provide enough space for vacuum housing and further cryogenic components. We used air-core coils (i.e. coils without FeCo in the teeth) as the magnetic flux density is so high that the FeCo would saturate and not help anymore with flux guidance. Further,

soft-magnetic teeth as usually known from electric machines, increase higher order harmonics in the stator field that give rise to increased losses in the cold rotor that we intent to avoid. For SPM designs with NeFeB all machines have typical teeth of FeCo. For comparison we calculated a SPM design with NeFeB and air-core coils. The magnetic air-gap for machines with teeth was 9 mm as a proper estimate for space to fit in the rotor bandage and have a mechanical air-gap of 3 mm.

The results of the pre-sizing are shown in table 2. For each machine type the depicted configuration represents the result of a manual optimization towards best power density under the assumptions given above and the constraints set by the specifications. The degrees of freedom that were used for optimization were the number of polepairs, number of slots, the machine's geometry (machine length, rotor diameter, magnet thickness, pole coverage angle, rotor yoke thickness, stator yoke thickness, teeth width, teeth height, teeth form) and the γ -angle. The maximum rotor diameter and magnet thickness were limited by a simple, analytical estimation of centrifugal forces.

The best variant for the inner rotor SPM has a active part power density of roughly 28 kW kg⁻¹. The outer rotor variant has roughly the same power density but at lower frequency. An interesting variant is number 4 where we decided to completely leave away the soft-material in the stator as the variant is an outer rotor design and therefore the field is shielded by the rotor from the outside (in order to fulfill the stray flux requirement $B_{stray} < 0.5$ mT): even though the airgap field is significantly reduced due to the higher magnetic resistance of air, still this design provides the best active part power density of 31 kW kg⁻¹ of all SPM machines. The machine designs with HTS-bulks with inner and outer rotor could offer an active part power density of 77 kW kg⁻¹ and 104 kW kg⁻¹, respectively. However, we used a Halbach configuration for the HTS-bulks where it is not clear if it is technically feasible or not. For wound field rotors an active part power density of 64 kW kg⁻¹ could be achieved. As this value is only slightly worse than the value for the HTS-bulk

inner rotor but the technology is far more familiar to us, we decided to go into the detailed design studies with this concept. An important note to make here is that the PM machines have a significantly lower power factor than the superconducting variants; hence requiring a bigger rectifier which would lead to a higher system mass in the end.

4. Detailed design

A CAD model of the detailed design that evolved in several iterations from the rough pre-sizing is shown in figure 1. The CAD model was created with the Siemens PLM Software Siemens NX 10.0.

The heart of the rotor are 16 HTS-coils that form 8 poles (i.e. 2 coils per pole) wound from HTS-tape such as referenced in [27, 28]. To hold them in place, they are glued into a coil carrier that can be made out of a metallic material such as aluminum or titanium. As the centrifugal forces are quite severe at 7000 rpm, the coil carrier is surrounded by an additional bandage that helps the coil carrier to withstand the centrifugal forces. As the coil-carrier (incl. bandage) is in direct contact with the HTS-coils it has also a temperature of 21 K. The first components that is at room temperature is the vacuum jacket of the rotor. Between the coil-carrier and the vacuum jacket is a thin vacuum gap of several mm that serves as thermal insulation. On the drive-end the vacuum jacket and the coil-carrier are connected by a torque-transmission element that transmits the torque from the HTS-coils through the coil carrier to the vacuum jacket. As it has to have high mechanical strength but also low thermal conductivity, materials such as CFK could be reasonable choice. Further the vacuum jacket is connected to the shaft on its outer side. To the shaft end the gas turbine would be connected. On the non-drive end the vacuum jacket has an inlet port (feed-through) through which liquid hydrogen can be inserted into the rotor. The liquid hydrogen feedthrough is a uniquely designed element that was elaborated by Siemens in prior projects and re-used for this design. For the bearings on the drive-end and non-drive end, we foresee standard industrial bearings such as can be found in [37].

Due to the air-coil winding also the stator has a non-conventional design configuration: the armature winding is realized as a two-layer distributed winding (for details section 4.1). Details of the electrical connections were not yet implemented at this design stage. As the FeCo yoke has no teeth the torque has to be transferred differently from the armature winding to the yoke (and further to the housing). For that purpose a GFK support structure is foreseen in which the armature winding is inserted. Towards the airgap the armature winding (with the support structure) is separated from the airgap by a slot pipe to realize the direct liquid cooling. The slot pipe is sealed by O-rings at both bearing shields so that the space between the slot pipe, the bearing shields and the housing is hermetically sealed. The torque is transferred from the support structure to the yoke by a form fit and from the yoke to the housing by a press-fit. The yoke material is FeCo and for the housing (and the bearing shields) a light-weight material such as aluminum can be used since the housing provides sufficient surface area so

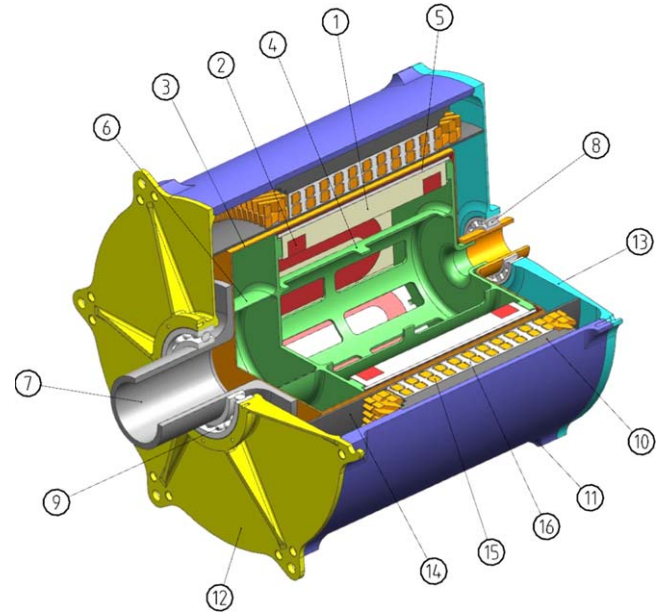


Figure 1. CAD model of the presented generator design. (1) Coil Carrier; (2) HTS-coil; (3) vacuum Jacket; 4 + (6) torque transfer elements; (5) bandage; (7) shaft; (8) NDE bearing; (9) DE bearing; (10) Stator yoke; (11) Housing; (12) DE Bearing shield; (13) NDE bearing shield; (14) slot pipe; (15) Armature winding; (16) stator support structure.

Table 3. Overview on important geometrical dimensions of the presented generator design.

HTS-pole height	27 mm
HTS-pole width	36 mm
HTS-pole length	306 mm
HTS minimal bending radius	21 mm
HTS maximum bending radius	37 mm
Rotor length	435 mm
Rotor inner radius	146 mm
Rotor outer radius	203 mm
Bearing distance	550 mm
Mechanical airgap	4 mm
Magnetic airgap	75 mm
Slot pipe thickness	4 mm
Amature winding inner radius	211 mm
Amature winding outer radius	255 mm
Stator yoke inner radius	255 mm
Stator yoke outer radius	280 mm
Stator yoke length	350 mm
Housing inner radius	280 mm
Housing outer radius	295 mm
Housing length	645 mm

that the torque could be transferred from the housing to a possible outer support structure without problems.

Important machine dimensions are summarized in table 3 and a mass decomposition of the important parts is given in table 4. The rotor has a total mass of roughly 148 kg and the stator a total mass of 274 kg. Largest contributors are the FeCo yoke and the armature winding. Although not all components

Table 4. Mass decomposition of important parts of the presented generator design.

HTS-coils	38 kg
Coil carrier	23 kg
Bandage	11 kg
Rotor cooling elements	4 kg
Vacuum jacket	11 kg
Torque transfer elements	15 kg
Shaft	14 kg
Drive-end bearing	5 kg
Non-drive-end bearing	25 kg
<i>Total rotor mass</i>	<i>148 kg</i>
Slot pipe	6 kg
Stator support structure	22 kg
Armature winding	57 kg
Stator yoke	112 kg
Housing	41 kg
Bearing shield NDE	8 kg
Bearing shield DE	13 kg
<i>Total stator mass</i>	<i>274 kg</i>
<i>Total generator mass</i>	<i>422 kg</i>

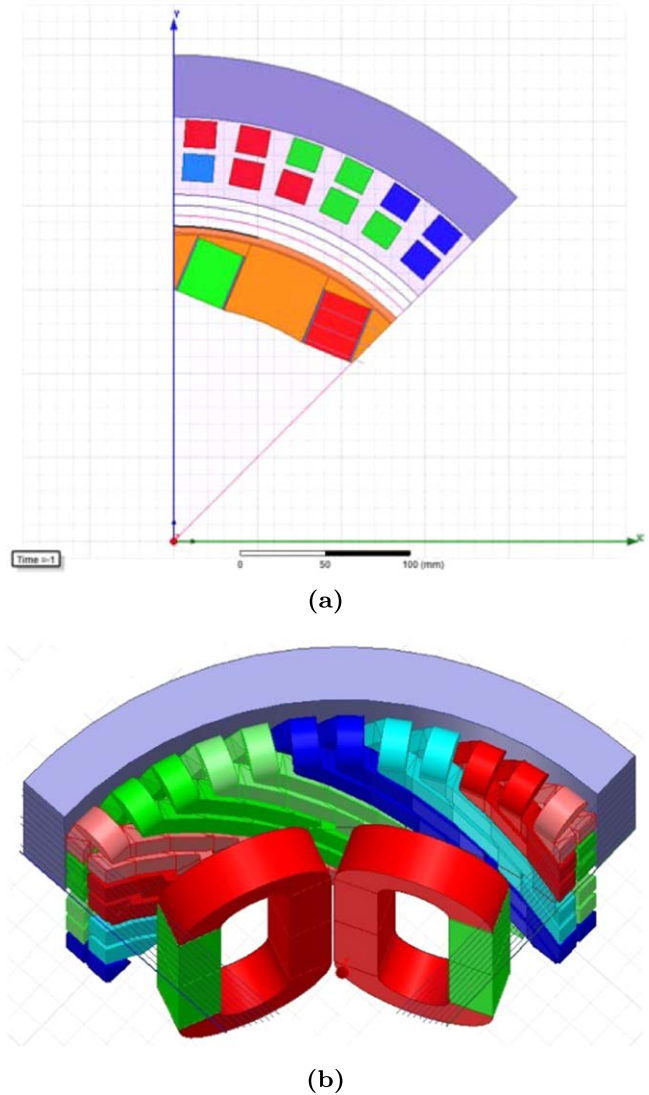
(such as bolts, connectors, vacuum ports, sensors, electrical feeds, etc) are included in the current design status and the included components have to be elaborated further into more detail, the total mass is clearly below 500 kg. Thus, we can state that a power density better than 20 kW kg^{-1} is feasible with this machine design since all design elements are backed by rigid calculations and experiments as described below.

4.1. Details of electromagnetic design

To evaluate important electromagnetic characteristics, we used 2D-FEM and 3D-FEM models. A cross-section of the 2D geometry can be seen in figure 2(a), a view of the simulated 3D geometry in figure 2(b). A summary of important electromagnetic machine characteristics resulting from these calculations is given in table 5. We would like to highlight that the machine has a high power factor of 0.89 which can be attributed to the fact that the machine has no teeth and also no soft-magnetic material in the rotor; resulting in a very low inductivity of $38 \mu\text{H}$ for an electric machine of this size.

As the power density is usually very sensitive to the number of pole pairs, we performed again an optimization concerning the pole pair number. The result is shown in figure 3. For each pole pair number there are several points which reflect the variation of important geometrical parameters such as machine length or yoke size. We see that the analytical pre-sizing is confirmed by FEM. While designs with 3 pole pairs have a worse power density, design with 5 pole pairs have a slightly better power density. However, higher pole pair number also increases the electric frequency which leads to higher AC losses and lower power factor. Thus, we decided to keep the 4 pole pair configuration for further calculations.

The magnetic field distribution within the machine for the optimized four-pole pair configuration is shown in figure 4. The magnetic field density is roughly 2.6 T in the center of each pole.

**Figure 2.** Electromagnetic FEM-calculation model in 2D and 3D.**Table 5.** Summary of electromagnetic characteristics of the presented generator design.

Effective power	10 MW
Apparent power	11.3 MVA
Power factor	−0.89
Torque	13.9 kNm
Rated effective coil current linkage	8451 A
Rotor current linkage	1.8 MA
Line-line peak voltage	3 kV
Power density (active parts)	48 kW kg^{-1}
Torque density (active parts)	67 Nm kg^{-1}
Tangential force density	17 N mm^{-2}
Esson utilization factor	$31.5 \text{ kVA min m}^{-3}$

In contrast to conventional machines with soft-magnetic teeth and rotor material, the magnetic airgap of our design is very large; it starts at the bottom of the yoke (opposite to one rotor pole) goes through two adjacent rotor poles and ends the bottom of the yoke

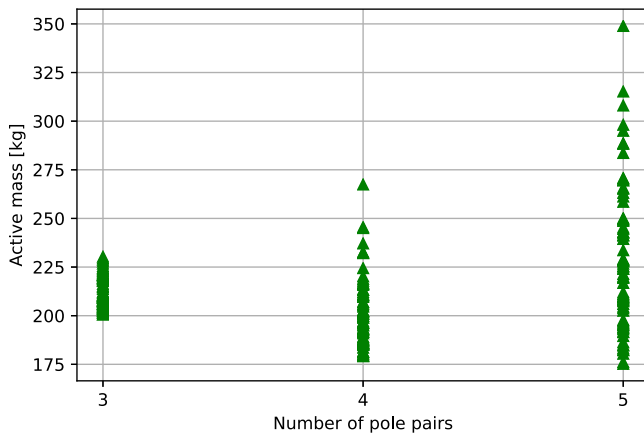


Figure 3. Mass dependence on pole pair number.

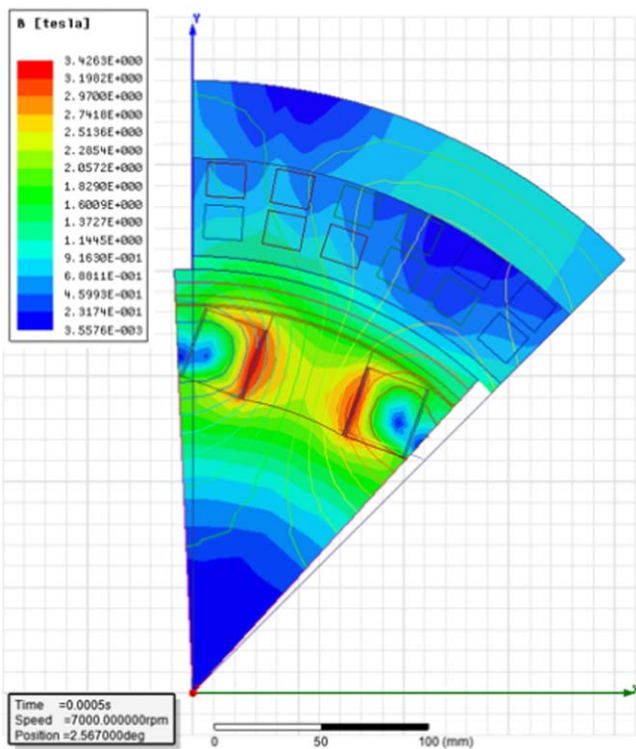
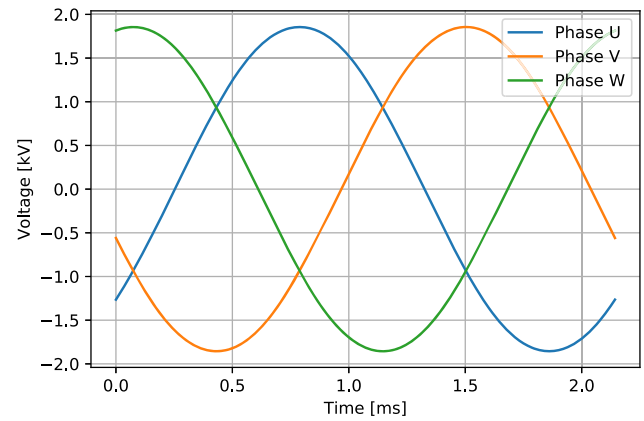


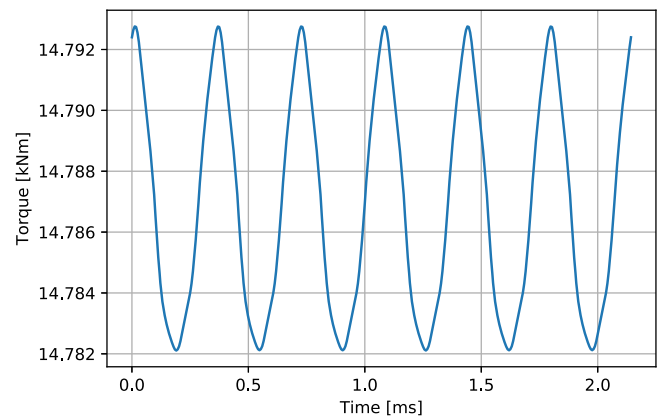
Figure 4. Magnetic flux density distribution computed with the 2D FEM model. The maximum field in the coil is around 3.5 T. In the coil center the magnetic flux density is around 2.6 T.

(opposite to the adjacent rotor pole). Thus, one cannot talk about the magnetic airgap field density but it declines gradually from roughly 1.5 T at the inner diameter of the armature winding to roughly 1 T at the inner diameter of the stator yoke. About 205 000 Ampereturns are required to produce this field.

These Ampereturns are realized by two HTS-coils on top of each other that have 205 turns each; feed with a current of 500 A (i.e. a current density of 250 A mm^{-2}). Comparing the magnetic field density and the current density to the B - J_c characteristics of a HTS-tape with good performance [27] shows that the HTS-tape should be able to work well with this current density. In order to be on the safe side regarding the angular dependency of the B - J_c characteristics, we evaluated the component of the magnetic field density that is perpendicular to the HTS-tape (i.e.



(a)



(b)

Figure 5. Induced voltage and transient torque computed with 3D FEM model. The torque ripple is below 1%.

parallel to the c -axis of the superconductor). The critical current degradation due to high magnetic fields is taken into account by having a safety margin of 50% to the critical current (i.e. $I_{\text{coil}}(B_{\text{max}}) \leq 0.5 I_c(B_{\text{max}})$, where B_{max} is the highest occurring magnetic flux density perpendicular to the HTS-tape surface). The HTS-tape we for see is 12 mm wide and has roughly $120 \mu\text{m}$ of metallic layers in between the superconducting layers. A thin insulating material such as Kapton is considered to be inserted between the turns. Geometrical dimensions of the coils are given in table 3. A detailed overview on the coil design was presented in [38].

The induced voltage for each phase and the torque are shown in figures 5(a) and (b). A harmonic analysis yields a relatively low torque ripple below 1% under full-load operation when fed with sinusoidal currents. Further, we used simulations to calculate the forces in the tangential and radial direction acting on the armature winding which is an important input for the structural analysis. The maximum force in radial directions is roughly 1.5 kN and in tangential direction 3.3 kN. For a machine of 10 MW these forces appear to be relatively low but one has to keep in mind, that the machine is a high speed machine wherefore a significant part of the power can be attributed to the rotation speed.

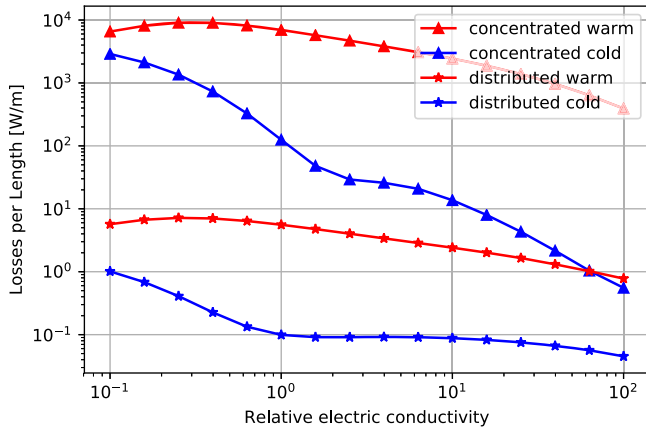


Figure 6. Electromagnetic losses in the rotor for a concentrated winding and a distributed winding as function of the relative electric conductivity of aluminum; 1 corresponds to $\sigma \approx 3 \times 10^5 \text{ S m}^{-1}$. The losses are several orders of magnitudes higher with a concentrated winding.

The armature winding is a two-layer distributed winding in helix configuration [39]³. We decided to go for this exotic winding configuration as we expect the winding heads to be more compact (and easier coolable) than with a classic distributed winding configuration. As the electric frequencies are high and the wire is fully exposed to the magnetic field, litz wire is necessary to get the AC losses under control. We chose litz-wire with a strand diameter of 0.4 mm so that AC-losses by skin-effect are neglectable. AC-losses by the proximity effect on strand and bundle level were calculated according to [40] and contribute additional 20% losses on top of the resistive losses. Losses in the yoke were extracted directly from the FEM simulation and contribute additional 4% on top. The winding consists of two three-phase systems. As a comparison between one three-phase system, a five-phase system and two three-phase systems showed that with two three-phase systems the torque can be increased by roughly 10%. Higher number of phases (7, 9 etc) did not show any significant gains in torque or harmonic reduction.

Despite the higher complexity in manufacturing we chose a distributed winding system over a concentrated winding. This decision can be attributed to substantially higher losses that are produced by the non-synchronous harmonics of the stator field induced into the rotor: in figure 6 the losses of the warm and cold parts of the rotor are shown as function of the relative electric conductivity of aluminum (1 corresponds to $\sigma \approx 3 \times 10^5 \text{ S m}^{-1}$) for a distributed winding and concentrated winding, respectively. With a distributed winding the losses at hydrogen temperature are roughly 70 W. The losses with a concentrated winding are about a factor of 1000 higher. With the intention to reduce the cold losses as much as possible as this will affect the mass of the cooling system later, the concentrated winding was rejected. The

losses in the HTS-tape were estimated analytically [41] and verified with 2D FEA simulations [42].

4.2. Details of thermal design

Although the target efficiency of 98% is very high, 2% of 10 MW are still 200 kW of heat which is dissipated inside of the stator. As the goal is to build a very light-weight and compact machine, the volume of heat decipation is small, resulting in a high heat power dissipation density (13 MW m^{-3}). We set the limits on the highest allowable temperatures to be

- (i) in the center of the litz-wire to be below 220°C . This is about 10°C below the point at which most litz-wire insulation material available on the market starts to degrege significantly.
- (ii) within the support structure below 200°C as above 200°C the mechanical properties degrege sensibly with increasing temperature.

A 1D CHT thermal network analysis reveals that both air jacket cooling and water air jacket cooling are not feasible concepts to keep the temperature within the required limits even if the mass-flow is very high. The reason for this is that the thermal resistance from heat source to the location where the heat is finally extracted from the machine is too high, in other words the thermal path is too long (given the thermal conductivity of the materials in use). A variation of the thermal conductivities in a range which appears challenging but maybe technologically feasible still does not provide a proper solution. Thus, a concept is required where the coolant is closer to the actual heat source. This can be realized if the winding is directly in touch with the coolant, i.e. with forced air or the stator has an inlet and an outlet for a liquid coolant that is pumped through the stator. The heat is directly transferred from the copper (where most losses are generated) to the coolant when it flows by the copper. We decided to go for a liquid coolant instead of forced air as liquids usually provide higher heat transfer coefficients. As the coolant liquid is in direct connect with the copper it has to be dielectric. After evaluation of several options we decided to go further with Novec7500 because it provides excellent thermal properties while still being reasonably safe. Its specification can be found in [43].

We evaluated this concept with 2D and 3D CHT simulations as well as with 3D CFD simulations. We used Siemens SimCenter NX Flow and Siemens SimCenter StarCCM+ for our calculations. The result of our 2D CHT simulation can be seen in figure 7: here the 2D cross-section of one copper bundle of one layer can be seen. In (a)–(c) the bundle is cooled from two sides, in (d)–(f) the bundle is cooled form all sides. Although the latter would in principle work thermally, the concept was disregarded due to mechanical design issues. Thus, when cooled from two sides, the litz-wire bundle has to have one additional spacing between the turns so that the bundle is separated in the center and the thermal path is halved. This can pose a difficult but not unsolvable challange for manufacturing.

We used a thermal conductivity of $\lambda = 1.4 \text{ W m}^{-1} \text{ K}^{-1}$ for the litz wire [44], a value which is not too conservative but also

³ Do not be confused that the stator winding configuration in the 2D FEM is not a helical but a 5/6. As the helical winding cannot be represented properly in a 2D FEM simulation, we decided to use a 5/6 winding instead. We chose a 5/6 configuration as it has a similar harmonics spectrum.

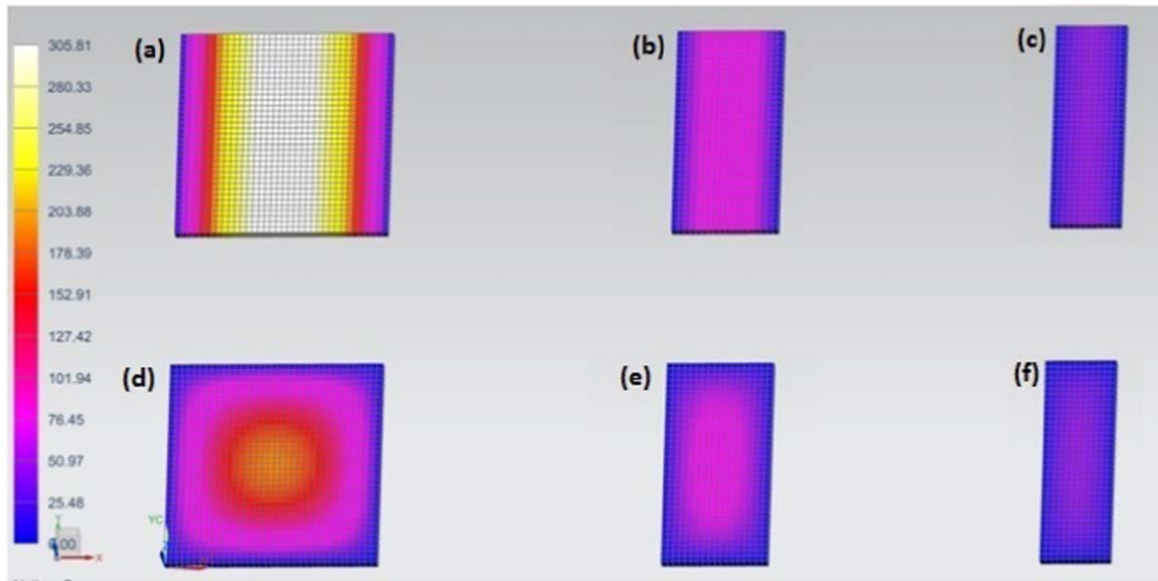


Figure 7. Temperature distribution within the litz bundles depending on the cooling geometry calculated with 2D CHT simulation: (a)–(c) cooling from four sides; (d)–(f) cooling from two sides. One separation of the litz bundle is required to achieve hot spot temperatures below the limit.

not too optimistic. According to [45] a fill factor of roughly 70% is required to achieve such values for the thermal conductivity, wherefore the litz wire that has normally a fill factor of 55%–60% has to be compressed further. For the heat transfer coefficient, we used a value of $\alpha = 3500 \text{ W m}^{-2}$ that we estimated with known analytical formulas from [46]. As the heat transfer coefficient is an important parameter for the heat extraction, we also determined it with CFD simulations for a geometry where the litzwire bundle is divided into two layers. The CFD simulation confirmed these values within range of 10%. The result of the CFD-simulation for one stator slot is shown in figure 8, where it can be seen that the temperature is fairly below the limits. The flowrates that are required to achieve these heat transfer coefficients are roughly 1000 l min^{-1} (for the complete machine). Although this value seems to be rather high, it is comparable to flow rates required for liquid cooled machines of similar size. The pressure drop with this flowrate for the total stator is lower than 1200 mbar.

The rotor cooling is conceived as a liquid hydrogen two-phase bath cooling. Hydrogen is inserted in liquid form through an insert pipe into the rotor. It is distributed over the rotor inner surface (i.e. over the coil carrier and the HTS-coils) due to the rotor's rotation. As the thermal conductivity of the coil carrier is rather high, the coils are not only cooled on the inner surface but also from the other sides due to conductive cooling through the coil carrier. Due to our experience from prior projects, the latent heat of hydrogen should provide sufficient cooling power if the cooling losses are below 500 W which is significantly below the calculated losses in the electromagnetic calculation. Additional losses can be expected due to radiation through the vacuum and the torque transfer element but also here, experience from previous projects suggests that these loss contributions are below the electromagnetic losses. As this kind of cooling concept

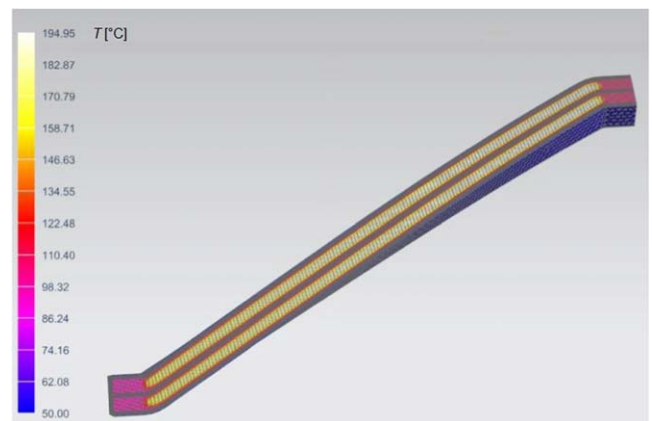


Figure 8. Temperature distribution within one slot calculated with 3D CFD. The highest temperature within the litz bundle is 195 °C; hence below the temperature limit.

Table 6. Summary of thermal aspects of the presented generator design regarding cooling.

Stator coolant	Novec7500
Volume flow rate	1000 l min^{-1}
Pressure drop	1200 mbar
Flow speed in channels	3.4 m s^{-1}
Number of cooling channels	192
Maximum stator coil temperature	195 °C
Maximum support structure temperature	120 °C

was successfully realized previously [16], we are confident that it would work well for the machine design that is presented in this work, too.

The results of the thermal design are summarized in table 6: Overall, we have a feasible cooling concept for the stator that is backed by simulations (and experiments) and a

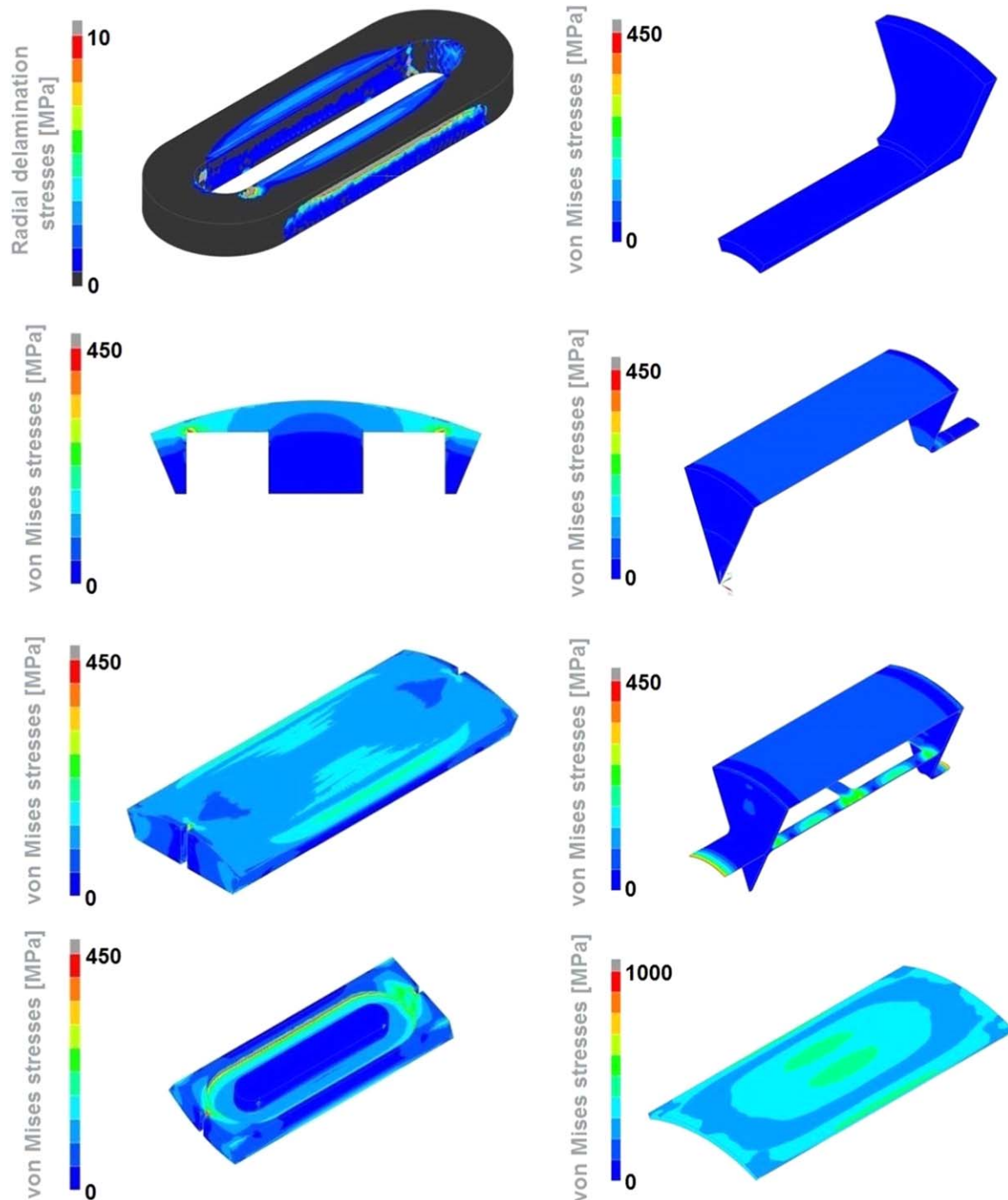


Figure 9. Stress state of the rotor parts (HTS-coil, coil carrier, bandage, shaft, torque transfer element and vacuum jacket) under 7000 rpm and 20 K.

feasible rotor cooling concept that is strongly supported by experience from prior projects. The resulting values from the simulations indicate that challenges in the domain of thermal management are difficult but doable.

4.3. Details of structure analysis

Due to the high rotation speed of the machine, the structural mechanical analysis of the machine is an important issue. Again rotor and stator have to be considered. We will start with the rotor considerations.

The loads on the rotor structure have the following contributions⁴:

- *Centrifugal loads:* Due to the rotation, centrifugal forces act onto the HTS-coils, the coil carrier, the sleeve and the vacuum jacket. Given a mass of ca. 2.4 kg per coil and a radius of 182 mm, the coil has a velocity of roughly 480 km h^{-1} at 7000 rpm. A rough analytical estimation of

⁴ Both for rotor and stator we neglect loads due to gravity as they are clearly neglectable.

the force, gives a value of 215 kN per coil, i.e. of 430 kN per pole and thus of 3440 kN for a total of eight poles.

- **Thermal loads:** As the rotor is assembled of many different materials at room temperature and then cooled down to about 20 K for operation, thermal loads arise. The thermal loads were taken into account by performing a thermal simulation ahead of the structural analysis.
- **Pressure loads:** Due to the centrifugal forces acting on the hydrogen due to the rotation, it exhibits a homogeneous, inner pressure of roughly 6 bar onto the coil carrier. This leads to a total surface force of roughly 275 kN.
- **Electromagnetic loads:** With a torque of roughly 13.9 kN m, and radius of 170 mm for the center of a pole, the force for eight poles in tangential direction is roughly 75 kN. Additionally there is a force of roughly 80 kN in radial direction derived from the electromagnetic simulations.

Clearly centrifugal loads and thermal loads are the major contributions to the mechanical stresses in the structure while electromagnetic forces and pressure forces can be neglected at first as their contributions is less than 10%. We evaluated the impact of these loads on the structure by means of 2D and 3D-FEM simulations. The simulations were performed with Siemens NX NASTRAN 10.0 and 11.0. After several iterations on the shape and the details of the geometry of the passive components (i.e. components that do not participate in the electromagnetic torque creation), we arrived at the presented geometry.

The result of the simulations for this design can be seen in figure 9: Looking into the different rotor parts from the outside to the inside shows, that the maximum stress in the bandage is below 700 MPa, thus close to the yield limit of material (830 MPa) but still below. Also, the maximum stress in the coil carrier which is 380 MPa is slightly below the yield limit of the material (410 MPa). The HTS-material is known to have anisotropic material properties [47, 48] as it has a composed laminate structure. It is much weaker in the direction of delamination. Thus, the maximum stress for the HTS-coil in delamination direction have to be checked. Indeed, it is at 8 MPa and hence slightly below the delamination level (10 MPa). Additionally, the strain level in the HTS-tapes has to be checked since it can affect the amperage of HTS-tape [49]. The maximum strain is at a level of 0.048‰, thus also below the level of critical current degradation.

In addition to the static load analysis, we also performed a rotor dynamics analysis in order to check if the rated speed is close to eigenmodes of the rotor. If that would be the case, it could lead to high vibrations and non-reversible damage to the machine. We used a simplified 3D-FEM model for our rotor dynamics analysis, where the coil carrier and the coils are regarded as one solid body and the roller bearings are applied as linear elastic elements at the corresponding locations.

In figure 10(a) the Campbell diagram and the corresponding modes of the critical speeds are visualized. There are two critical modes that are between 0 and 7000 rpm. We see

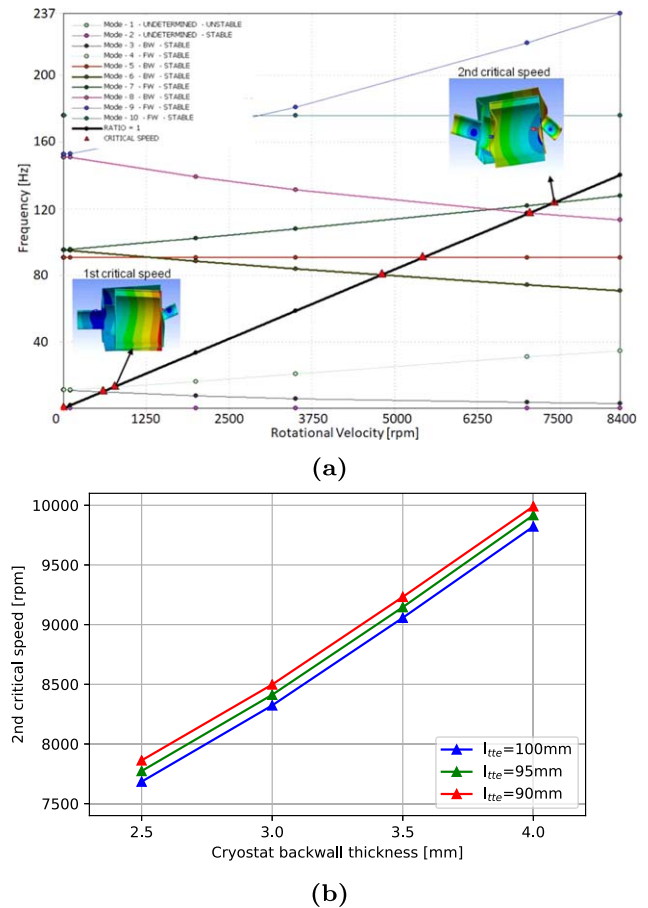


Figure 10. Result of rotor dynamics simulation. Critical speeds can be seen in the campbell diagram (a) at 771 rpm and 7402 rpm. As can be seen in (b) the second critical speed can be detuned by reasonable changes in the geometrical parameters.

that one eigenmode is clearly below the operation speed (at 771 rpm) and one is really close (7402 rpm). We see that one mode arise due to the fact that the coil carrier is fixed only on one side to the shaft (on the drive-end) and another is related to the cryostat wall thickness. As we want the critical mode to be at least 20% away from the rated speed, we checked to which geometrical parameters the eigenmode frequencies are most sensitive in order to detune them. As stated above, the 2nd mode is most sensitive to the cryostat wall thickness. In figure 10(b) the frequency of the 2nd critical mode is shown as a function of cryostat wall thickness. We see that by increasing the wall thickness from about 2.5–4 mm (which is a feasible design change) we can increase the frequency to be 20% above the rated speed. The mode at 771 rpm can hardly be detuned to be above the operation range. Therefore, one has to go quickly through this speed and operate the machine overcritically.

The loads on the stator structure have the following two contributions:

- **Electromagnetic loads:** Due to the electromagnetic forces, radial and tangential forces act directly onto the armature winding. In contrast to classical machines with soft-magnetic teeth, the volume of attack for the forces is not the soft-magnetic material but the copper itself, wherefore

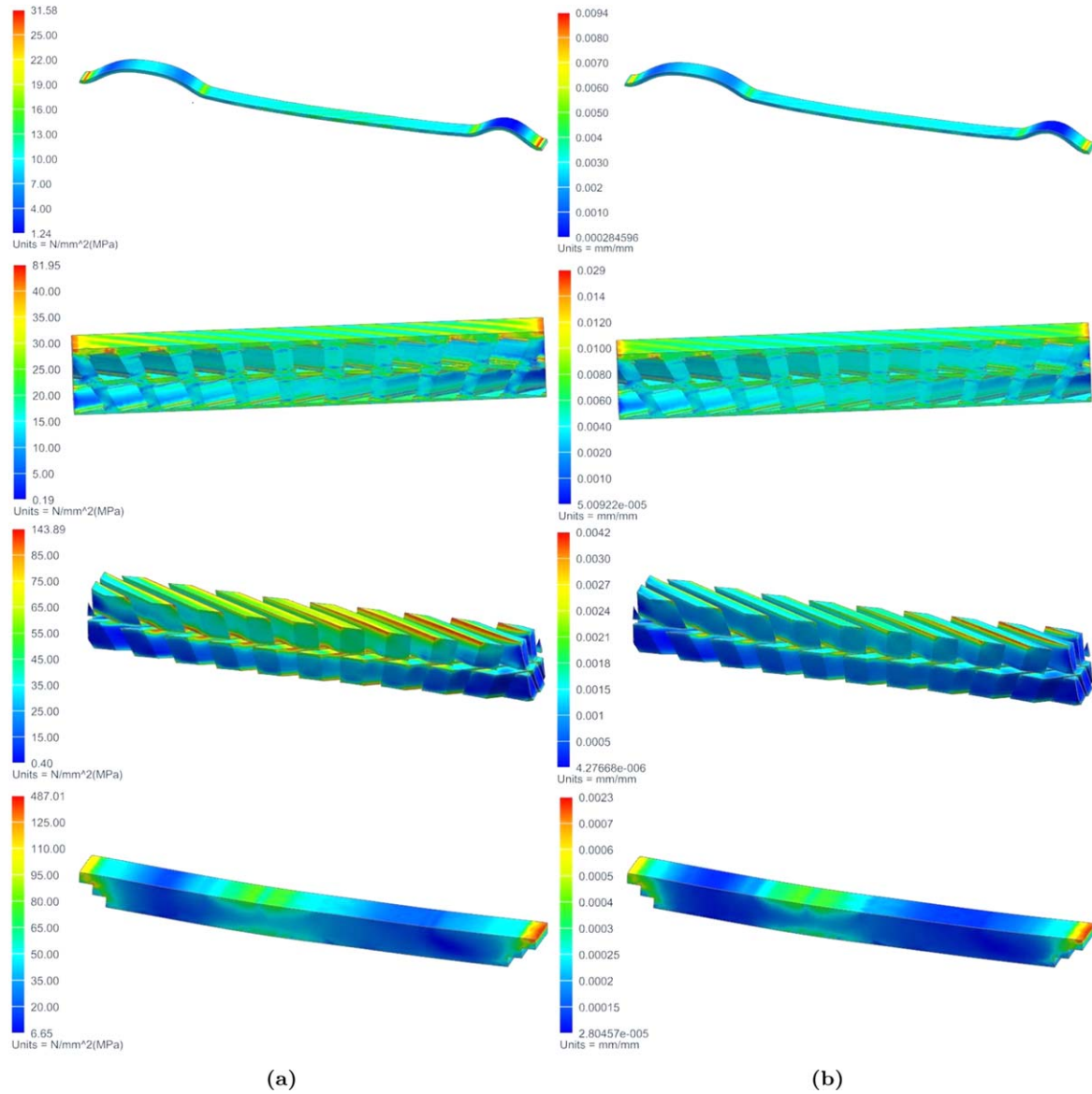


Figure 11. Stress (a) and strain (b) in the stator components (slot pipe, support structure, armature winding, yoke).

the forces are transferred from the copper to the laminate structure and then through the yoke to the housing.

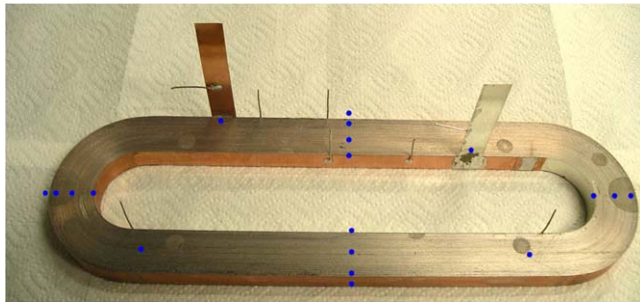
- **Thermal loads:** The stator consists of several materials all of which have different thermal expansion coefficients. Further, the generator is assembled at room temperature and during operation the litz-wire temperature is roughly 150 °C, while the ambient temperature of the housing is at 55 °C. Due to the complexity of the geometry it was hardly possible to make an analytical estimation of the thermal loads and they were directly calculated in as a part of the FEM simulation.

Again, we performed 3D FEM simulations to analyze the resulting stress and strain in the stator parts under the loads described above. The stress results are shown in figure 11(a): The stresses in the yoke are at a level of 110 MPa, therefore clearly under the yield stress of the material (460 MPa). The stress within the armature winding is 75 MPa which is close to the yield strength of copper (80 MPa). However, the winding, made out of compressed litz wire, is a complex 3D-structure of

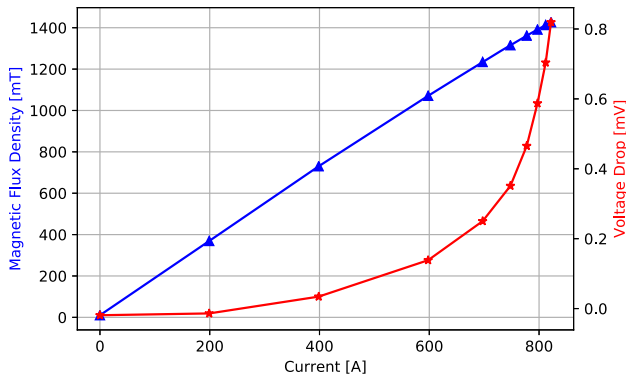
copper and isolation material in-between. Hence, the mechanical properties of this structure have to be measured in future to gain higher confidence in its structural integrity within the stator. Nevertheless, as the armature winding is embedded into the laminate structure and impregnated later, we are confident that it will operate well under the given mechanical loads. The strain within the laminate structure is shown in figure 11(b): the strain within the laminate structure are at a level of 2.53% which is below the strain load limit of typical laminate materials (3%) that could be used.

5. Tests and further challenges

Although the digital twin that we created for our design gives us a high level of confidence in its technical feasibility, we decided to check the most critical issues for each design discipline by dedicated experiments.



(a)



(b)

Figure 12. Example of manufactured test coil (a) and the corresponding measured B – I curve (b).

5.1. High performance HTS excitation coils

Our design requires high performance HTS-coils that are compact (i.e. have a small bending radius and small turn height) and produce high magnetic field flux densities at the same time. As a small bending radius can decrease the HTS-tape performance, we manufactured and tested several HTS-coils in order to make sure that the designed HTS-coils can achieve the required performance indeed. Our prototype coils had dimensions according to the design outlined in section 4. The photography of a coil prototype after manufacturing is shown in figure 12(a). We used several HTS-tapes to test the coil manufacturing which all worked well concerning the manufacturing process.

We characterized the coils at 77 and 21 K. For the characterization we measured the magnetic field density in the center of the coil as a function of the current. The result is shown in figure 12(b): the measured B – I dependency is within roughly 2% accuracy in correspondence with our simulations. Thus, we regard the manufacturing experiments as successful and the HTS-coil design as feasible.

5.2. Structural integrity of rotor design

The structural material utilization of the parts in the rotor is close to the material limits, wherefore we decided to assure the design by rotation test in a spin bunker. For that test we built a 1:2-scale prototype. We used the same material for the passive components as intended for the full scale design,

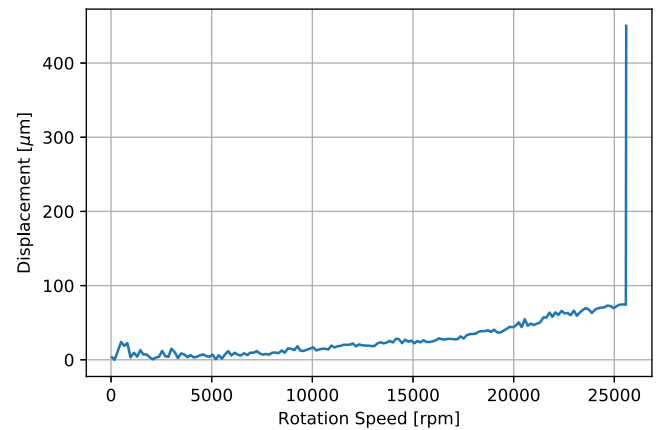


Figure 13. Results of the speed bunker test. The disintegration of the rotor can be seen clearly in the data at 25 500 rpm.

i.e. the coil-carrier was made out of aluminum and the bandage of titanium. As the purpose of the experiment is pure structural mechanics, we did not use expensive HTS-material but a material of similar density for the coils. The experimental specimen did not have a vacuum jacket as its material utilization is not critical.

The specimen was rotated in a spin bunker until it bursted. Results from strain gauges placed on the specimen's surface are shown in figure 13: they indicate that plastical deformation started at 16 800 rpm until the specimen bursted at 25 500 rpm. These results with the 1:2-scale rotor demonstrate that the proposed rotor design is feasible concerning structural design.

5.3. Validation of CFD results and assumptions

Concerning thermal management most uncertainty comes from the heat transfer coefficient α that was extracted from CFD calculations and the assumptions on the thermal heat conductivity λ . Concerning the heat transfer coefficient, we performed an experiment where cooling channels such as foreseen between the litz-wire bundles were emulated. Novec7500 was pumped with different inlet temperature and flow rates through a structure that reassembles the geometry of the stator design. The walls are heated with similar values as would be expected from the machine losses. The temperature of the coolant at the beginning and the end of the geometry is measured, as well as the pressure drop. From the temperature measurement and the knowledge of the geometry, the heat transfer coefficient is extracted. Results of the experiments are shown in figure 14. We see that in reality the thermal performance is in general in good agreement with the simulation concerning the heat transfer. Also, the pressure drop is lower than predicted wherefore higher flowrates than anticipated could be realized. Overall, it gives us confidence that the thermal management of the machine is doable.

Further, we measured the thermal conductivity of litz-wire specimen with two methods: Laser flash and guarded hot-plate. For a litz-wire configuration as we foresee it in our design we measured a value $3.1 \text{ W m}^{-1} \text{ K}^{-1}$ with both methods in good correspondence. This value is better than the

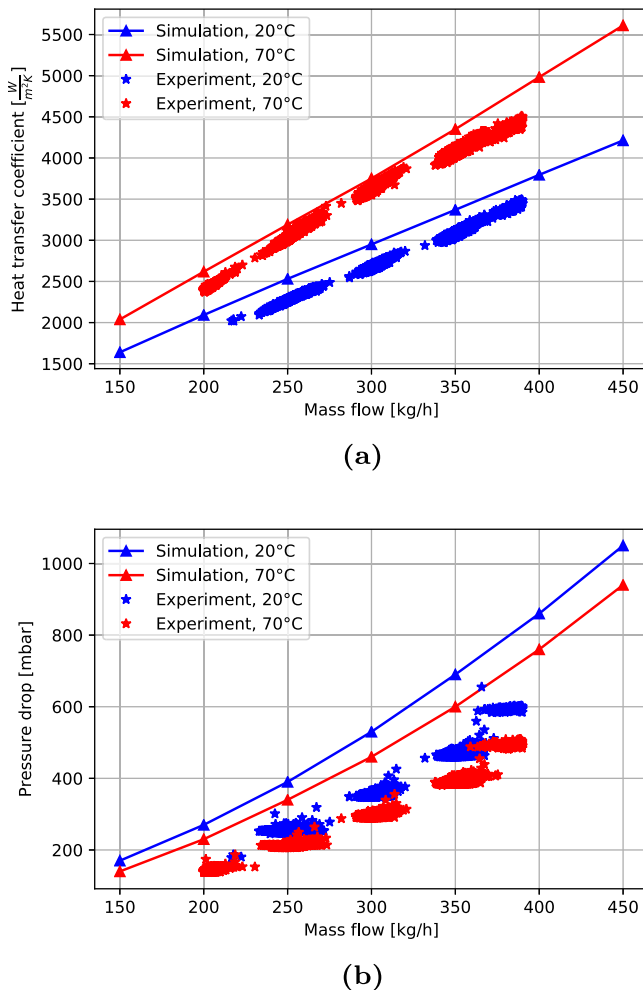


Figure 14. A comparison between analytical calculation, CFD simulation and experiment. The heat transfer coefficient is in good agreement between simulation and experiment. The pressure drop turns out to be lower in reality than initially calculated.

assumption of the simulation, therefore giving us further confidence in the feasibility of the concept.

Towards an actual flyable generator, we see further challenges in particular in the following areas:

- Several parts in the rotor are permanently exposed to hydrogen. These are in particular the HTS-coils and the coil-carrier. It is well known that the mechanical properties of materials are affected by hydrogen embrittlement [50]. Further, it can be assumed that also the superconducting properties might be affected by a similar mechanism [51]. While for a ground prototype or for single permit-to-flight demonstration this might not pose a significant constraint, it might largely affect the mid- and longterm operation. Hence, the effect of hydrogen embrittlement on the HTS-tapes and the corresponding coil-carrier material has to be studied in detail.
- Compared to industrial high power electric generators, the materials in the stator are exposed to frequencies that are 10 times higher at a much higher material utilization. Thus, the material properties of compressed litz-wire and

of the corresponding laminate materials have to be investigated in detail concerning high cycle fatigue.

- Although high voltage insulations of 3 kV are not untypical for high power electric machines on the multi-MW power level, the goal of light-weight designs means that conventional insulation systems can hardly be reused. As for high power densities, the thermal utilization has to be driven to its limits and a good electrical insulation is typically also a good thermal insulation, the insulation poses a high thermal resistance. As discussed in section 4.2, the thermal resistance has to be reduced and therefore also the electrical insulation. A very thin electric insulation will work but will not be partial discharge free below a particular thickness, thus limiting the life-time of the stator. Therefore, for proper mid- and longterm operation, qualification of high performance electrical insulation systems is required.
- Not at last, a detailed investigation of safety aspects is necessary. In this paper we covered the technical feasibility of achieving very high power densities but did not provide an in-depth discussions of safety aspects. Such must include the behavior under different short-circuit scenarios, HTS-failure, rotor cooling system failure, stator cooling system failure, operation with a single winding system and several other failure scenarios. Although the generator does not have to be fail-safe under all possible failure aspects, it is important to know how these could be handled in case of emergency.

6. Conclusions

In this paper we presented the design studies for a 10 MW HTS-generator for direct coupling to an airborne gas-turbine. With the digital twin of the full machine that covers all the relevant physical disciplines, we come to a conclusion that a dry-weight below 500 kg, i.e. a power density beyond 20 kW kg^{-1} is achievable. This is possible if HTS-tapes are used in the rotor as excitation coils as they enhance the magnetic field density beyond what is achievable with the best permanent magnets. A high level comparison shows that this is roughly 2–3 times better to what can be achieved with SPM machines under similar requirements and constraints. Also, the power factor for superconducting machines is expected to be significantly better, therefore lowering the total system weight. Although, further aspects such as details of manufacturing, safety aspects and material qualification have to be addressed in future, in order to realize actual flyable products, our result clearly demonstrate the outstanding potential of HTS for very lightweight multi-MW electric machines.

Acknowledgments

We would like to thank the Bundesministerium für Wirtschaft (BMWi) and the Deutsches Zentrum für Luft- und Raumfahrt (DLR) for providing the TELOS project (grant number 20Y1516C) that was the foundation for conducting this

research project. Also, we would like Frank Palm, Frederick Berg and Peter Rostek from Airbus Innovations for an open and fruitful technical discussion. We would like to thank Karsten Brach and Christian Bauer from Siemens AG as well as Professor Ulrich Werner from TH Nuremberg for valuable discussions on electromagnetics, mechanical design and rotordynamics. Not at last we would like the numerous colleagues and supplier companies who helped us greatly to calibrate our digital twin.

ORCID iDs

Mykhaylo Filipenko  <https://orcid.org/0000-0002-9187-5720>

References

- [1] 2007 IATA calls for a zero emission future (<https://iata.org/en/pressroom/pr/2007-06-04-02/>)
- [2] 2011 *Flightpath 2050: Europe's Vision for Aviation* European Commission (<https://ec.europa.eu/transport/sites/transport/files/modes/air/doc/flightpath2050.pdf>)
- [3] Epstein A H 2014 Aeropropulsion for commercial aviation in the twenty-first century and research directions needed *AIAA J.* **52** 901–11
- [4] Schäfer A W, Barrett S R H, Doyme K, Dray L M, Gnadt A R, Self R, O'Sullivan A, Synodinos A P and Torija A J 2019 Technological, economic and environmental prospects of all-electric aircraft *Nat. Energy* **4** 160–6
- [5] Schulz E 2018 *Global Networks, Global Citizens 2018-2037* (Toulouse: Airbus S.A.S.) (<https://airbus.com/content/dam/corporate-topics/publications/media-day/GMF-2018-2037.pdf>)
- [6] Höelzen J, Liu Y, Bensmann B, Winnefeld C, Elham A, Friedrichs J and Hanke-Rauschenbach R 2018 Conceptual design of operation strategies for hybrid electric aircraft *Energies* **218** 11
- [7] Stückl S, van Toor J and Lobentanzer H 2012 Voltair—the all electric propulsion concept platform—a vision for atmospheric friendly flight *Proc. 28th Int. Congress of the Aeronautical Sciences* pp 1–12
- [8] Thielmann A, Sauer A, Isenmann R and Wietschel M 2018 Technology roadmap energy storage for electric mobility 2030
- [9] Jansen R H, Brown G V, Felder J L and Duffy K P 2015 Turboelectric aircraft drive key performance parameters and functional requirements *Proc. 53rd AIAA/SAE/ASME Joint Propulsion Conf., AIAA Propulsion and Energy Forum*
- [10] Kuhn H, Seitz A, Lorenz L, Isikveren A T and Sizmann A 2012 Progress and perspectives of electric air transport *Proc. 28th Int. Congress of the Aeronautical Sciences*
- [11] Durrell J H *et al* 2014 A trapped field of 17.6 T in melt-processed, bulk Gd–Ba–Cu–O reinforced with shrink-fit steel *Supercond. Sci. Technol.* **27** 082001
- [12] Ballarino A and Flickinger R 2017 Status of MgB₂ wire and cable applications in europe *IOP Conf. Ser.: J. Phys.* **871** 012098
- [13] Zhou D, Izumi M, Miki M, Felder B, Ida T and Kitano M 2012 An overview of rotating machine systems with high-temperature bulk superconductors *Supercond. Sci. Technol.* **25** 103001
- [14] Matsuzaki H, Kimura Y, Ohtani I, Izumi M, Ida T, Akita Y, Sugimoto H, Miki M and Kitano M 2005 An axial gap-type HTS-bulk synchronous motor excited by pulsed-field magnetization with vortex-type armature copper windings *IEEE Trans. Appl. Supercond.* **15** 2222–5
- [15] Nick W, Grundmann J and Frauenhofer J 2012 Test results from siemens low-speed high-torque HTS machine and description of further steps towards commercialisation of HTS machines *Physica C* **482** 105–10
- [16] Nick W, Frank M, Klaus G, Frauenhofer J and Neumüller H-W 2007 Operational experience with the world's first 3600 rpm 4 MVA HTS generator *Proc. ASC 2006* vol 17, pp 2030–3
- [17] Bergen A, Andersen R, Bauer M, Boy H, ter Brake M, Brutsaert P, Bühler C, Dhalle M, Hannsen J and ten Kate H 2019 Design and in-field testing of the world's first ReBCO rotor for a 3.6 MW wind generator *Supercond. Sci. Technol.* **32** 125006
- [18] Snitchler G, Gamble B and Kalsi S 2005 The performance of a 5 MW high temperature superconductor ship propulsion motor *IEEE Trans. Appl. Supercond.* **15** 2206–9
- [19] Gieras J F 2009 Superconducting electrical machines state of the art *Prz. Elektrotech.* **85** 1–19
- [20] Haran K S *et al* 2017 High power density superconducting rotating machines-development status and technology roadmap *Supercond. Sci. Technol.* **30** 123002
- [21] Perez A, van der Woude R R and Decker R 2019 Rotor cooling concept for the ASuMED superconductive motor *IOP Conf. Ser.: Mater. Sci. Eng.* **502** 012139
- [22] Sivasubramaniam K, Laskaris E T and Bray J W 2007 High power density HTS iron core machines for marine applications 2007 *IEEE Power Engineering Society General Meeting*
- [23] Jansen R H, Jesus-Arce Y D, Kascak P, Dyson R, Woodworth A, Scheidler J, Edwards R, Stalcup E and Wilhite J 2018 High efficiency megawatt motor conceptual design *Joint Propulsion Conf., AIAA Propulsion and Energy Forum and Exposition*
- [24] Jansen R H, Brown G V and Duffy K P 2017 Partially turboelectric aircraft drive key performance parameters *Proc. 53rd AIAA/SAE/ASME Joint Propulsion Conf., AIAA Propulsion and Energy Forum*
- [25] Berg F, Palmer J, Miller P, Husband M and Dodds G 2015 HTS electrical system for a distributed propulsion aircraft *IEEE Trans. Appl. Supercond.* **25** 1–5
- [26] 1995 DIN VDE 0848-4, Sicherheit in elektromagnetischen Feldern—Schutz von Personen im Frequenzbereich von 0 bis 30 kHz, Änderung A3, 1995 (<https://vde-verlag.de/normen/0848006/din-v-vde-v-0848-4-a3-vde-v-0848-4-a3-1995-07.html>)
- [27] Daibo M 2019 Recent progress of 2G HTS wires and coils at Fujikura (<https://conference-indico.kek.jp/indico/event/62/contribution/22/material/slides/0.pdf>)
- [28] Tsuchiya K *et al* 2017 Critical current measurement of commercial REBCO conductors at 4.2 K *Cryogenics* **85** 1–7
- [29] Binder Andreas 2012 *Elektrische Maschinen und Antriebe* (Berlin: Springer)
- [30] Walter H, Bock J, Frohne C, Schippl K, May H, Canders W R, Kummeth P, Nick W and Neumueller H W 2006 First heavy load bearing for industrial application with shaft loads up to 10 kN *J. Phys.: Conf. Ser.* **43** 995–8
- [31] Zhou D, Ainslie M D, Srpic J, Huang K, Shi Y, Dennis A R, Cardwell D A, Durrell J H, Boll M and Filipenko M 2018 Exploiting flux jumps for pulsed field magnetisation *Supercond. Sci. Technol.* **31** 105005
- [32] 2016 Vacuumschmelze: Soft magnetic cobalt-iron alloys vacoflux and vacodur datasheet (www.vacuumschmelze.de)
- [33] 2018 Yasa P400 R series product sheet (https://yasa.com/wp-content/uploads/2018/01/YASA_P400_Product_Sheet.pdf)
- [34] Kleimaier A and Hoffmann B 2011 Axial flux motor DYNAX—a compact electric drive for automotive power trains *Proc. 1st Int. Electric Drives Production Conf.*
- [35] Bause R, Ainslie M D, Corduan M, Boll M, Filipenko M and Noe M 2019 Electromagnetic design of a superconducting electric machine with bulk HTS material arXiv:1903.08906

- [36] 2016 Shin Etsu N39UH Nd–Fe–B magnet demagnetization curves at elevated temperature (<http://www.shinetsu-rare-earth-magnet.jp/e/download/N39UHsheet.pdf>)
- [37] INA FAG. Zylinderrollenlager, 2006
- [38] Oomen M 2019 HTS rotor coils and joints for high power density rotating machines *European Conf. on Applied Superconductivity*
- [39] Conley P L, Kirtley J L, Hagman W H and Ula A H M S 1979 Demonstration of a helical armature for a superconducting generator *Proc. IEEE PES Summer Meeting* p 716ff
- [40] Albach M, Patz J, Roßmanith H, Exner D and Stadler A 2010 Optimale wicklung = optimaler wicklungsgrad *Elektronik Power* 38–46
- [41] Oomen M 2000 AC loss in superconducting tapes and cables *PhD Thesis* University of Twente, Enschede
- [42] Grilli F 2009 Numerical modelling of HTS applications *IEEE Trans. Appl. Supercond.* **26** 0500408
- [43] 2018 3M Novec 7500 engineered fluid product information (<https://multimedia.3m.com/mws/media/65496O/3mtm-novectm-7500-engineered-fluid.pdf>)
- [44] Wrobel R, Ayat S and Baker J 2017 Analytical methods for estimating equivalent thermal conductivity in impregnated electrical windings formed using litz wire *Proc. IEEE Int. Electric Machines and Drives Conf.*
- [45] Simpson N 2013 Estimation of equivalent thermal parameters of impregnated electrical windings *IEEE Trans. Ind. Appl.* **49** 2505–15
- [46] 2013 *VDI Wärmeatlas* (Berlin: Springer)
- [47] Diev D N, Anashkin O P, Keilin V E, Krivykh A V, Polyakov A V and Shcherbakov V I 2014 Delamination tests of 2G HTS tapes at room and liquid nitrogen temperatures *AIP Conf. Proc.* **1574** 245
- [48] Yujie G Y D and Wurui T 2018 Numerical models of delamination behavior in 2G HTS tapes under transverse tension and peel *Physica C* **545** 26–37
- [49] Igarashi M, Fujita S, Sato H, Iijima Y, Naoe K, Nagata M, Tateno F and Daibo M 2016 Y-based coated conductors for high-field applications *Fujikura Tech. Rev.* 1–5
- [50] Ambat R and Dwarakadasa E S 1996 Effect of hydrogen in aluminium and aluminium alloys: a review *Bull. Mater. Sci.* **19** 103–14
- [51] Chandra J and Manekar M A 2019 Effect of hydrogen loading on superconducting properties of niobium *AIP Conf. Proc.* **2115** 030507